

Free-space quantum key distribution to a moving receiver

Jean-Philippe Bourgoin,^{1,2} Brendon L. Higgins,^{1,2} Nick Gigov,^{1,2} Catherine Holloway,^{1,2}
Christopher J. Pugh,^{1,2} Sarah Kaiser,^{1,2} Miles Cranmer,^{1,2} and Thomas Jennewein^{1,2,3}

¹*Institute for Quantum Computing, University of Waterloo, Waterloo, ON N2L 3G1, Canada*

²*Department of Physics and Astronomy, University of Waterloo, Waterloo, ON N2L 3G1, Canada*

³*Quantum Information Science Program, Canadian Institute for Advanced Research, Toronto, ON, Canada**

Technological realities limit terrestrial quantum key distribution (QKD) to single-link distances of a few hundred kilometers. One promising avenue for global-scale quantum communication networks is to use low-Earth-orbit satellites. Here we report the first demonstration of QKD from a stationary transmitter to a receiver platform traveling at an angular speed equivalent to a 600km altitude satellite, located on a moving truck. We overcome the challenges of actively correcting beam pointing, photon polarization and time-of-flight. Our system generates an asymptotic secure key at 40 bits/s.

Contemporary communications security relies on assumptions about an adversary's computational ability, a property that is uncontrolled and can rapidly change over time. In contrast, quantum key distribution (QKD) provides a mechanism to establish future-proof secure communications between two parties by exploiting fundamental quantum mechanics to generate a secret, random encryption key common to both parties [1]. While commercial application of this technology is growing, with current technology direct QKD links cannot reach distances beyond a few hundred kilometers due to optical losses [2–6]. Quantum repeaters [7, 8] promise to be an essential component of future long-distance QKD networks, but such devices are not ready for operational integration [9, 10]. Alternatively, an orbiting satellite could serve as an untrusted node [11, 12]—linking two ground stations simultaneously and facilitating key distribution without acquiring the key itself—or as trusted node [13–19]—exchanging individual keys with each ground station and broadcasting the combination of two keys to allow two ground stations to establish a shared key. Although the satellite is privy to the keys, by requiring only one link at a time the trusted node satellite benefits from a simpler design and, with a suitable orbit, allows key distribution between two parties located anywhere on Earth.

A satellite QKD link will require optical pointing mechanisms compatible with the requirements of a quantum link—i.e., capable of preserving the quantum information while maximizing the average transmission (but not necessarily the signal consistency required for classical optical communication). Recent demonstrations of QKD using moving transmitters [20, 21] imitate the case of a transmitting satellite platform, albeit without a traveling platform reaching the angular speed of a satellite, but a satellite-based quantum receiver is somewhat less complex to develop, and adds flexibility to utilize multiple different source technologies, including attenuated laser pulses and entangled photons [22]. To show the viability of such an approach, we demonstrate an optical QKD link to a moving receiver platform, traveling at equivalent angular speed of a satellite, supported by automated compensation of polarization drifts in the fiber (including drifts due to the movement of the tracking system) from the source to the

transmitter, and a coincidence algorithm incorporating time-of-flight correction.

Our QKD receiver (Bob) is located in the cargo area of a pickup truck driven along a road approximately 650m from the transmitter (Alice)—see Figure 1. To maintain the link we utilize 850 nm wavelength beacon lasers and CMOS cameras, in conjunction with a tracking algorithm operating at 24 Hz, at both transmitter and receiver. Over the link we transmit intensity- and polarization-modulated pulses, implementing BB84 QKD with decoy states [23]. Simultaneously, the truck maintains an angular speed exceeding the maximum angular speed of a typical low-Earth-orbit (LEO) satellite platform [22], thereby supporting the feasibility of performing QKD from a ground station to an orbiting satellite.

QKD states are generated by a weak coherent pulse (WCP) source located in a ground-floor laboratory in the Research Advancement Center 1 building on the University of Waterloo campus. Our WCP source produces photon pulses at 532 nm wavelength through sum-frequency generation (SFG), combining an 80 MHz pulsed 810 nm Ti:sapphire laser with a continuous wave (CW) 1550 nm laser that is intensity and polarization modulated using fiber-based electro-optical intensity and phase modulators [24]. The resulting 532 nm pulses possess the same pulse rate and pulse width (≈ 0.5 ps) as the Ti:sapphire laser while having the same polarization as the CW laser.

The 532 nm pulses are sent to the transmitter (Figure 2, left) via an optic fiber, where they are collimated to a beam with ≈ 10 mm waist by a 1-inch diameter, 30 mm focal-length lens. Following this, to correct for phases and rotations arising from the fiber transmission (which vary in time due to temperature fluctuations in the building), the transmitter is equipped with a polarization characterization and compensation system. We use a modified optical chopper where upon each of six open slots has been placed a polarizer aligned to pass horizontal (H), vertical (V), diagonal (D), antidiagonal (A), right- (R), or left-circular (L) polarization. Some of the closed slots of the chopper wheel were removed to improve signal transmission. As a result, 50% of the signal pulses pass the chopper wheel unobstructed, 20% are polarized (either absorbed or passed, with probability dependent on the

state overlap with the orientation of the polarizer) and the remaining 30% are blocked. A beam-splitter is used to send 10% of the unobstructed signals to a multi-mode fiber which is coupled to a single-photon detector. The proportions of detected polarized signals are assessed each second and used to tomographically characterize the states at the transmitter. To return the measured states to the desired H, V, D, and A polarization states for QKD transmission, we optimize a theoretical model of a set of wave plates in rotation mounts, consisting of two quarter-wave plates on either side of a half-wave plate. We then apply the optimized rotations to actual wave plates mounted in motorized rotation stages. With this, in contrast to other polarization alignment approaches [25–27], we are able to compensate, prior to the QKD signal leaving the telescope, *any* phase or rotation which may be induced by the fiber, directly applying a unique compensation solution at all times. (Although other approaches are suitable for alignment between the transmitter and receiver frames [26, 27], the receiver frame was inherently sufficiently aligned to the transmitter for our demonstration.)

The receiver (Figure 2, right) consists of a 2-inch diameter input lens (100mm focal length) followed by a 6.5 mm diameter collimating lens (11 mm focal length). A beam-splitter is used to implement a passive basis choice between the H/V basis (reflected port) and the D/A basis (transmitted port). The polarization measurement is performed using 10mm polarizing beam-splitter cubes (PBS). An extra PBS (rotated 90° around the beam path) is added at the reflected port of each measurement PBS to suppress noise. In each of the four measurement outputs, the light is focused into multi-mode fibers (105 μm core diameter) using a 1-inch diameter, 60mm focal-length collection lens and a 12.5 mm diameter, 100mm focal-length focusing lens. The four fibers are connected to silicon avalanche photodiodes which detect the photons. The field of view of the receiver is 0.02°. The receiver platform is suspended on the truck with a small inner-tube and held in place with sliding metal bars and elastic straps.

The transmitter and the receiver are each mounted on an orthogonally oriented pair of rotation stages, one with a horizontal (azimuth) axis of rotation and the other with a vertical (elevation) axis of rotation. On each motorized platform, a camera and three beacon lasers are included, allowing for the transmitter and receiver to each use the other’s beacon signal deviation, measured on their camera, to control their motors. The pointing algorithm is based on velocity estimation of the beacon spot on the camera and its deviation from a nominal center, and adjusts the velocity of the motors to match the estimated velocity plus a proportional error term to reduce the deviation. Both of these corrections are based on a weighted average (exponentially decaying) of previous spot velocity estimates, in order to suppress high frequency jitter.

The size of the optical spot at the receiver had a measured diameter of about 12cm. Following link acquisition, the total link loss at the receiver averaged 30.6dB, mostly due to geometric effects, with other effects—including atmospheric transmittance, detector efficiency and losses in optical

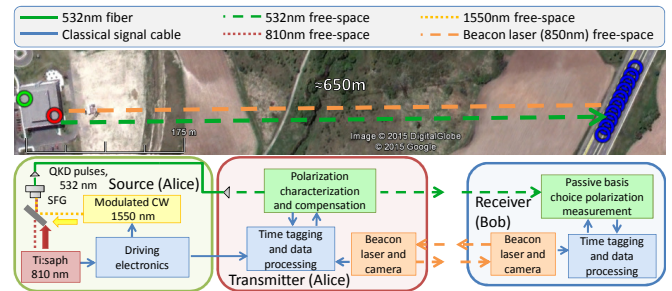


FIG. 1: Schematic overview of the moving receiver experimental setup with map showing the location of Alice, consisting of the source (green circle) and transmitter (red circle), and the section of the road that Bob, located on the truck, traveled (blue circles, one per second) during the moving receiver tests. Signals from the source (located in the laboratory on the ground floor of the building) are sent to the transmitter using an optical fiber. An active laser beacon-tracking pointing system is used to maintain the free-space link while the truck is traveling, and a wireless local area network (WLAN) is used for classical communications. The distance from the transmitter to the truck is $\approx 650\text{m}$ and the length of the road traveled during the test was $\approx 80\text{m}$. Map data: Google, DigitalGlobe.



FIG. 2: Alice transmitter (left) and Bob receiver (right) apparatuses. The transmitter produces a $\approx 10\text{mm}$ beam and includes a chopper wheel with polarizer films followed by a 10% reflective beam splitter with a fiber coupler in the reflected port, allowing us to tomographically characterize the polarization state of some of the transmitted photons. This characterization allows us to implement, in real time using a set of motorized wave plates, a compensation to the polarization drift of the states caused by the fiber to the transmitter. Only the signals that passed through the open slots of the chopper wheel are used for key generation. The receiver, which is mounted on the back of a pickup truck, implements a passive basis choice photon polarization measurement.

components—accounting for only 7dB of loss. We calculate that the geometric effects contribute 12dB loss from diffraction alone, with an average of 4.3dB of additional loss due to pointing error of the transmitter and atmospheric turbulence, and an average of 7.3dB loss from the receiver pointing error. The receiver pointing error contributes more loss than the transmitter because road and motor-induced vibrations of the truck under motion result in increased jitter. These vibrations would be absent on a satellite platform.

During the experiment the truck is driven at a speed of 33 km/h, corresponding to an angular speed of $0.75^\circ/\text{s}$, above the maximum angular speed of a LEO satellite platform at 600km altitude: $0.72^\circ/\text{s}$ at zenith. Calculated using per-

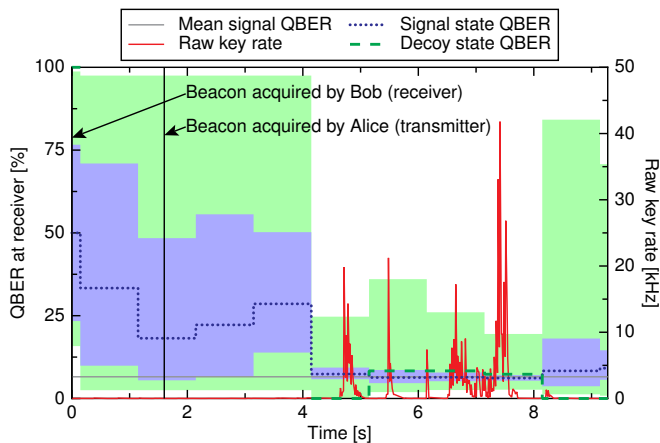


FIG. 3: QBER and count rate measured at the receiver. The horizontal gray line represents the mean signal QBER of the data selected for the QKD protocol (6.55%). The shaded regions around the QBERs correspond to a 95% central credible interval. The QBER drops when the count rate increases at 4s to 8s. The large range of the credible interval of the decoy QBER is due to the low number of measured decoy states, with results near the beginning absent as no decoy states were measured at those times. The measured values are taken with a 0.16ns coincidence window, with the QBER measured on a per second basis and the counts measured on a 2ms basis.

second GPS coordinates, we observe a time-of-flight variation of around 15 ns/s, which we correct with linear interpolation. (See Supplementary Information for more details.) A satellite time-of-flight variation, which could be as high as 20 ms/s near the horizon (approaching zero at zenith, where the count rates are highest), could be corrected similarly, but may require a finer correction, e.g. a higher-order interpolation incorporating predicted orbital positions. Figure 3 shows the signal quantum bit error ratio (QBER), the decoy QBER, and the count rate during the test. The count rate increases once the link stabilizes after initial acquisition (which takes ≈ 4 s), briefly reaching over 41 kHz. Even after acquisition, there remains a large amount of fluctuations due to the low pointing accuracy of the receiver, which varies outside the 0.02° field of view of the receiver. Both the signal and decoy QBER decrease as the counts increase, with a minimum measured signal QBER of 6.16%.

Intrinsic QBER of the source is the primary contributor to the measured QBER. We indirectly measure the intrinsic QBER via the polarization compensation system, which measures the polarization states arriving at the transmitter and predicts those states after the optimized correction is applied by the wave plates. The measured QBER before compensation and the predicted QBER after compensation are shown in Figure 4. Before compensation, the QBER varies around 10% to 13%, increasing over the duration of the test, while the predicted QBER after compensation stays constant at around 6%. We conclude that the measured QBER at the receiver—6.5% to 8% when the count rate is above 1000—is mostly caused by the intrinsic QBER found at the transmitter, with

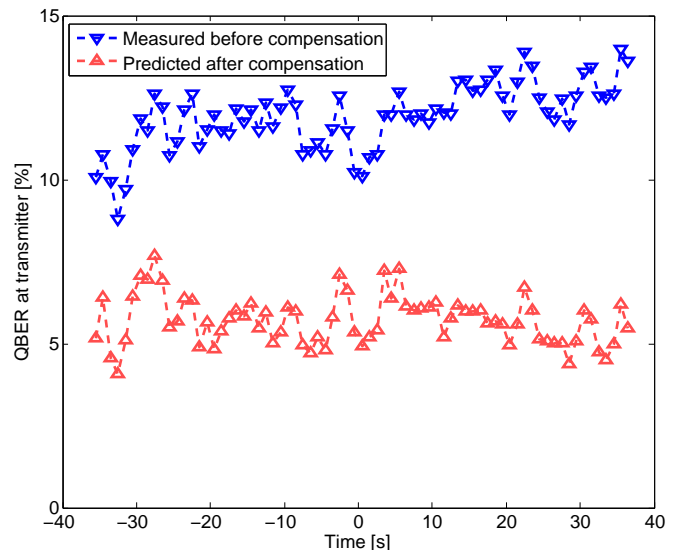


FIG. 4: Measured pre-compensation and predicted post-compensation QBER at the exit of Alice’s transmitter. The time origin corresponds to the start of the optical signal acquisition. The polarization compensation system corrects the unitary induced by the fiber from the source to the transmitter and returns the polarization states to near their intrinsic QBER of $\approx 6\%$.

the additional 0.5% to 2% owing to background noise at the receiver. Following the completion of the experiment, modelling showed that this QBER is largely due to reduced purity, efficiency imbalance between the two SFG crystals, and deviations in the modulator phase for two polarization states (see Supplementary Information).

We examine the 4s of data where the counts within each second total more than 1000, effectively applying a signal-to-noise filter [28]—a filter with finer grain could potentially improve the results, given the high frequency fluctuations of the count rate (Figure 3). From these data, we extract 160 bits of secure key, not considering finite-size statistical effects. A longer link duration would be required in order to extract secure key when including finite-size statistics—to extract secure key with finite-size statistics to ten standard deviations (a common heuristic [29]), a total of 13210s of data at the measured system performance would be required. Improvement to the intrinsic QBER of the system could drastically reduce this link duration requirement. For example, in a similar system we recently demonstrated QKD at high loss, showing an asymptotic key rate of 1.79 Mbit/s at a loss of 35.5 dB [30] (4.9 dB above the measured 30.6 dB of our system), while QBERs of $< 1\%$ have previously been achieved in other WCP QKD sources [26].

The asymptotic-limit result of our experiment is sufficient to show the viability of QKD to a moving receiver platform travelling at an angular speed of up to $0.75^\circ/\text{s}$. Of course, the useful optical contact time to a satellite (within a single pass) is limited to only a few hundred seconds. However, given sufficiently precise tracking, key extraction while accounting for

finite-size fluctuation is nevertheless feasible under this limited time [22, 30].

We have thus demonstrated the feasibility of using a moving receiver platform for QKD. We constructed a custom pointing system, and used it to maintain a free-space quantum link over which BB84 decoy-state quantum signals were exchanged to a truck traveling at angular speeds consistent with a LEO satellite, sufficient to generate asymptotically secure key. With reasonable improvements to the system, such as reducing the source intrinsic QBER, and the addition of a second-stage fine-pointing mechanism (both of which are largely engineering challenges with demonstrated solutions) we expect to achieve appreciable secure key bit rates with the inclusion of finite-size statistics. Such improvements will also allow us to demonstrate QKD to a moving receiver over longer distances and higher losses, completing necessary steps towards achieving long-distance satellite-mediated QKD networks.

Acknowledgments

The authors would like to thank Christian Barna, Alexander Chuchin and Jennifer Fernick for assistance during the experimental tests. Support for this work by CFI, CIFAR, CryptoWorks21, CSA, FedDev Ontario, Industry Canada, Ontario Research Fund and NSERC is gratefully acknowledged. S.K. acknowledges support from Mike & Ophelia Lazaridis Fellowship.

* Electronic address: jbourgoin@uwaterloo.ca, thomas.jennewein@uwaterloo.ca

- [1] V. Scarani, H. Bechmann-Pasquinucci, N. J. Cerf, M. Dušek, N. Lütkenhaus, and M. Peev, *Rev. Mod. Phys.* **81**, 1301 (2009).
- [2] R. Ursin, F. Tiefenbacher, T. Schmitt-Manderbach, H. Weier, T. Scheidl, M. Lindenthal, B. Blauensteiner, T. Jennewein, J. Perdigues, P. Trojek, B. Oemer, M. Fuerst, M. Meyenburg, J. Rarity, Z. Sodnik, C. Barbieri, H. Weinfurter, and A. Zeilinger, *Nature Physics* **3**, 481 (2007).
- [3] D. Stucki, N. Walenta, F. Vannel, R. T. Thew, N. Gisin, H. Zbinden, S. Gray, C. R. Towery, and S. Ten, *New J. Phys.* **11**, 075003 (2009).
- [4] Y. Liu, T.-Y. Chen, J. Wang, W.-Q. Cai, X. Wan, L.-K. Chen, J.-H. Wang, S.-B. Liu, H. Liang, L. Yang, C.-Z. Peng, K. Chen, Z.-B. Chen, and J.-W. Pan, *Opt. Exp.* **18**, 8587 (2010).
- [5] Z. Yan, D. R. Hamel, A. K. Heinrichs, X. Jiang, M. A. Itzler, and T. Jennewein, *Rev. Sci. Instrum.* **83**, 073105 (2012).
- [6] R. H. N. G. M. J. L. D. N. B. S. B. Korzh, C. C. W. Lim, R. Thew, and H. Zbinden, *Nature Photonics* **9**, 163 (2015).
- [7] C. H. Bennett, G. Brassard, C. Crépeau, R. Jozsa, A. Peres, and W. K. Wootters, *Phys. Rev. Lett.* **70**, 1895 (1993).
- [8] H.-J. Briegel, W. Dür, J. I. Cirac, and P. Zoller, *Phys. Rev. Lett.* **81**, 5932 (1998).
- [9] C. Simon, M. Afzelius, J. Appel, A. B. de la Giroday, S. J. Dewhurst, N. Gisin, C. Y. Hu, F. Jelezko, S. Kröll, J. H. Müller, J. Nunn, E. S. Polzik, J. G. Rarity, H. de Riedmatten, W. Rosenfeld, A. J. S. N., Sköld, R. M. Stevenson, R. Thew, I. A. Walmsley, M. C. Weber, H. Weinfurter, J. Wrachtrup, and R. J. Young, *The European Physical Journal D* **58**, 1 (2010).
- [10] N. Sangouard, C. Simon, H. de Riedmatten, and N. Gisin, *Rev. Mod. Phys.* **83**, 33 (2011).
- [11] R. J. Hughes, W. T. Buttler, P. G. Kwiat, S. K. Lamoreaux, G. L. Morgan, J. E. Nordholt, and C. G. Peterson, in *Aerospace Conference Proceedings, 2000 IEEE*, Vol. 1 (2000) pp. 191–200 vol.1.
- [12] Z. Tang, R. Chandrasekara, Y. Y. Sean, C. Cheng, C. Wildfeuer, and A. Ling, *Scientific Reports* **4**, 6366 (2014).
- [13] W. T. Buttler, R. J. Hughes, S. K. Lamoreaux, G. L. Morgan, J. E. Nordholt, and C. G. Peterson, *Phys. Rev. Lett.* **84**, 5652 (2000).
- [14] J. E. Nordholt, R. J. Hughes, G. L. Morgan, C. G. Peterson, and C. C. Wipf, *Free-Space Laser Communication Technologies XIV* **4635**, 116 (2002).
- [15] J. G. Rarity, P. R. Tapster, P. M. Gorman, and P. Knight, *New J. Phys.* **4**, 82 (2002).
- [16] R. Ursin, T. Jennewein, J. Kofler, J. M. Perdigues, L. Cacciapuoti, C. J. de Matos, M. Aspelmeyer, A. Valencia, T. Scheidl, A. Acin, C. Barbieri, G. Bianco, C. Brukner, J. Capmany, S. Cova, D. Gigenbach, W. Leeb, R. H. Hadfield, R. Laflamme, N. Lütkenhaus, G. Milburn, M. Peev, T. Ralph, J. Rarity, R. Renner, E. Samain, N. Solomos, W. Tittel, J. P. Torres, M. Toyoshima, A. Ortigosa-Blanch, V. Pruneri, P. Villoresi, I. Walmsley, G. Weihs, H. Weinfurter, M. Zukowski, and A. Zeilinger, *Europhysics News* **40**, 26 (2009).
- [17] R. Etengu, F. M. Abbou, H. Y. Wong, A. Abid, N. Nortiza, and A. Setharaman, *J. Opt. Commun.* **32**, 37 (2011).
- [18] R. Hughes and J. Nordholt, *Science* **333**, 1584 (2011).
- [19] E. Meyer-Scott, Z. Yan, A. MacDonald, J.-P. Bourgoin, H. Hübel, and T. Jennewein, *Phys. Rev. A* **84**, 062326 (2011).
- [20] S. Nauerth, F. Moll, M. Rau, C. Fuchs, J. Horwath, S. Frick, and H. Weinfurter, *Nature Photonics* **7**, 382–386 (2013).
- [21] J.-Y. Wang, B. Yang, S.-K. Liao, L. Zhang, Q. Shen, X.-F. Hu, J.-C. Wu, S.-J. Yang, H. Jiang, Y.-L. Tang, B. Zhong, H. Liang, W.-Y. Liu, Y.-H. Hu, Y.-M. Huang, B. Qi, J.-G. Ren, G.-S. Pan, J. Yin, J.-J. Jia, Y.-A. Chen, K. Chen, C.-Z. Peng, and J.-W. Pan, *Nature Photonics* **7**, 387–393 (2013).
- [22] J.-P. Bourgoin, E. Meyer-Scott, B. L. Higgins, B. Helou, C. Erven, H. Hübel, B. Kumar, D. Hudson, I. D’Souza, R. Girard, R. Laflamme, and T. Jennewein, *New J. Phys.* **15**, 023006 (2013).
- [23] W. Y. Hwang, *Phys. Rev. Lett.* **91**, 057901 (2003).
- [24] Z. Yan, E. Meyer-Scott, J.-P. Bourgoin, B. L. Higgins, N. Gigov, A. MacDonald, H. Hübel, and T. Jennewein, *J. Lightwave Technol.* **31**, 1399 (2013).
- [25] J. Chen, G. Wu, Y. Li, E. Wu, and H. Zeng, *Opt. Express* **15**, 17928 (2007).
- [26] M. Toyoshima, H. Takenaka, Y. Shoji, Y. Takayama, M. Takeoka, M. Fujiwara, and M. Sasaki, *International Journal of Optics* **2011**, 254154 (2011).
- [27] M. Zhang, L. Zhang, J. Wu, S. Yang, X. Wan, Z. He, J. Jia, D. S. Citrin, and J. Wang, *Opt. Exp.* **22**, 9871 (2014).
- [28] C. Erven, B. Heim, E. Meyer-Scott, J.-P. Bourgoin, R. Laflamme, G. Weihs, and T. Jennewein, *New J. Phys.* **14**, 123018 (2012).
- [29] S.-H. Sun, L.-M. Liang, and C.-Z. Li, *Phys. Lett. A* **373**, 2533 (2009).
- [30] J.-P. Bourgoin, N. Gigov, B. L. Higgins, Z. Yan, E. Meyer-Scott, A. Khandani, N. Lütkenhaus, and T. Jennewein, (2015), in preparation.

Free-space quantum key distribution to a moving receiver: Supplementary Information

Jean-Philippe Bourgoin,^{1,2} Brendon L. Higgins,^{1,2} Nick Gigov,^{1,2} Catherine Holloway,^{1,2}
 Christopher J. Pugh,^{1,2} Sarah Kaiser,^{1,2} Miles Cranmer,^{1,2} and Thomas Jennewein^{1,2,3}

¹*Institute for Quantum Computing, University of Waterloo, Waterloo, ON N2L 3G1, Canada*

²*Department of Physics and Astronomy, University of Waterloo, Waterloo, ON N2L 3G1, Canada*

³*Quantum Information Science Program, Canadian Institute for Advanced Research, Toronto, ON, Canada**

RESULTS

The angular deviation of the motor positions, as measured by the imaged beacon spot on the camera, is shown in Figure 1. Initial acquisition and stabilization required approximately 4 s following first acquisition of the beacon. The mean deviation after stabilization of the link was measured to be 0.005° at the transmitter and 0.06° at the receiver. The extra deviation at the receiver is due to the jitter from the vibrations of the truck. (A pointing test with the truck stationary showed similar mean deviation to the measured transmitter deviation, 0.005° , at both parties.) Figure 2 shows the angular velocity of the motors during the test. Both the transmitter and the receiver averaged an azimuthal angular speed above $0.72^\circ/\text{s}$, with the transmitter (Alice) showing a more consistent angular speed.

The time of flight (Figure 3) is calculated from per-second GPS coordinates recorded during the experiment, and is subtracted from detection event times assuming a linear time-of-flight variation and extrapolating the position of the truck from the most recent per-second data using the velocity, also given

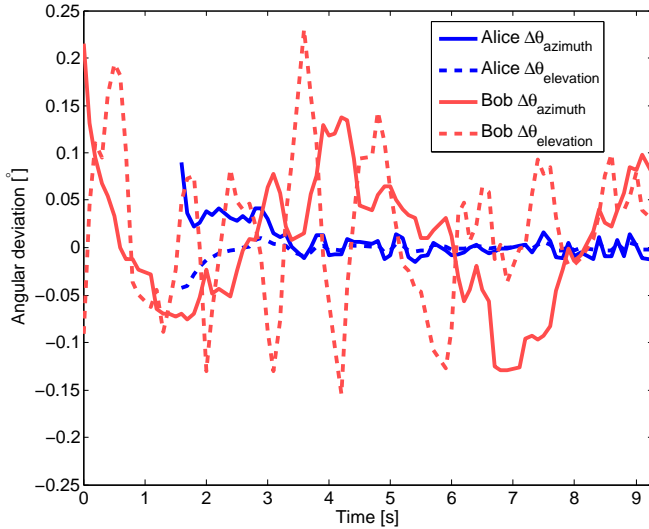


FIG. 1: Beacon angular deviation measured by the camera. The reported deviation on Alice (Bob) is the angular deviation of Bob’s (Alice’s) beacon as seen by Alice’s (Bob’s) camera. The increase in variation at the receiver (Bob) can be attributed to the instabilities produced by the motion of the truck. The transmitter (Alice) shows increased deviation in the azimuthal axis, caused by the jitter in the mounting frame which can move more easily in the horizontal plane than the vertical plane.

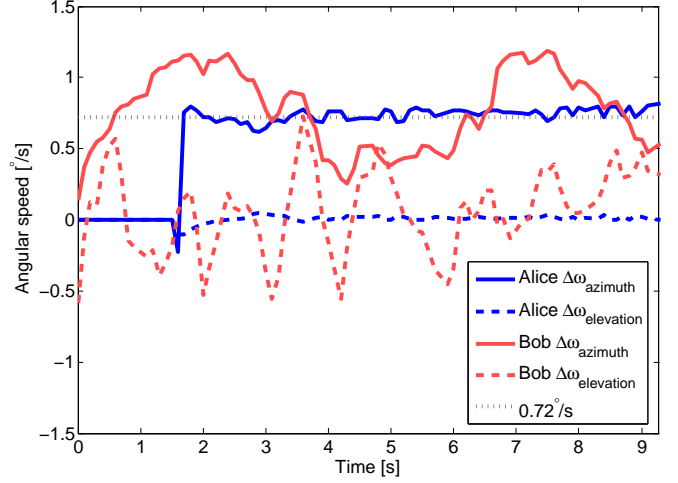


FIG. 2: Angular speed of the motors during the 30 km/h test. The gray dotted line represents the maximum angular speed of a 600 km LEO satellite ($0.72^\circ/\text{s}$). The higher variation at the receiver (Bob) is due to jitter and curving motion of the truck. The azimuthal angular speed at the transmitter (Alice) is more consistent, with only a small increase (of $\approx 0.03^\circ/\text{s}$) during the test. Before 1.6 s Alice’s motors are not moving because she has yet to acquire Bob’s beacon signal.

by the GPS receiver. Post-processing steps, including error correction and privacy amplification, are performed after the transmission, and secure key is extracted. The measured QKD parameters are reported in Table I.

SOURCE INTRINSIC QBER

A detailed analysis of the intrinsic QBER of the source was performed to determine the origin of the excessive QBER. This analysis was performed using measured state data obtained from the polarization compensation system. The per-second tomographic reconstruction gives us density matrices of the polarization states at the transmitter. From these density matrices we calculate the purity and fidelity of the states at the transmitter, shown in Table II. The mean purity and fidelity of the states was found to be 91 % and 94 % respectively.

To determine the origin of the intrinsic QBER, we modeled the various components of the source acting on the initial diagonally polarized state, ρ_D , at the input of the modulator system. The phase modulators apply a phase on the vertical component of the input state, dependent on the desired state. This operation is modeled as the unitary operation (ignoring

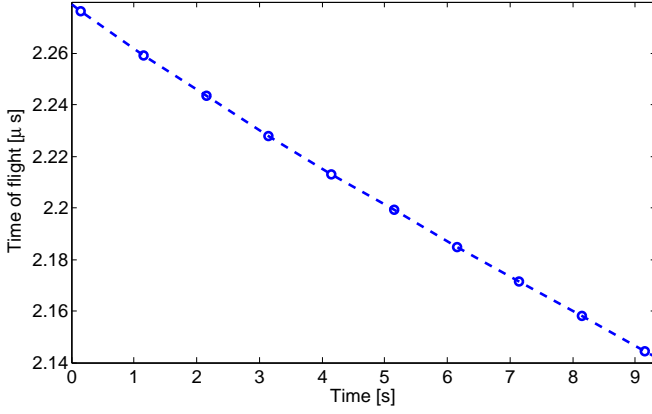


FIG. 3: Time of flight from the transmitter to the receiver calculated from GPS coordinates. The time of flight changes almost linearly and can thus be effectively compensated using a first order linear time-of-flight correction.

TABLE I: Experimentally measured QKD parameters of the moving receiver test. The parameters are based on a 0.16 ns coincidence window using data where the received counts exceeded 1000 cps. The small window allows us to increase the signal-to-noise ratio (and thus reduce the QBER) at the cost of reduced raw key rate.

Parameter	Value
Duration	4 s
Signal average photon number	0.495
Decoy average photon number	0.120
Signal QBER	6.55 %
Decoy QBER	5.49 %
Signal gain	5.86×10^{-5}
Decoy gain	1.5×10^{-5}
Single photon gain lower bound	3.72×10^{-5}
Single photon QBER upper bound	5.85 %
Vacuum yield	1.35×10^{-7}
Average loss	30.6 dB
Error correction efficiency	1.15
Raw key length	11477 bits
Sifted key length	5844 bits
Secure key length (asymptotic)	160 bits
Secure key bit-string	01001010100010101011 00100110010001111010 00011100000000010000 10000000101111101111 01000001110100110101 10010011000001001001 10001100100001111111 00010111101111101011

global phase terms),

$$U_{\text{ph},x} = \begin{bmatrix} 1 & 0 \\ 0 & e^{i\phi_x} \end{bmatrix}, \quad (1)$$

written in the H/V basis, with ϕ_x being the phase applied for the desired output state $x \in \{\text{H}, \text{V}, \text{D}, \text{A}\}$. The phase modulators are in an interferometric configuration [1] which may

possess a transmission imbalance. This imbalance, which we parametrize by the angle θ_{mod} , is modeled as

$$U_{\text{mod}} = N_{\text{mod}} \begin{bmatrix} \cos \theta_{\text{mod}} & 0 \\ 0 & \sin \theta_{\text{mod}} \end{bmatrix}. \quad (2)$$

This operation represents differing losses in the H and V modes, and is thus non-unitary. Because we are only concerned with the properties of states that are ultimately measured, we renormalize to impose unit total probability in both modes via the N_{mod} factor. Note that this factor is dependent on the state at this stage.

Because the interferometer cannot directly produce H and V, but only states on the Bloch circle passing through D, A, R and L, a unitary rotation operation is then applied to the state to transform R to H and L to V:

$$R = \frac{1}{\sqrt{2}} \begin{bmatrix} 1 & -i \\ -i & 1 \end{bmatrix}. \quad (3)$$

After the modulators, the signal traverses an optic fiber guided to the SFG apparatus. The fiber applies some unitary rotation on the state, which we model as a general SU(2) unitary,

$$U_a = \begin{bmatrix} \cos(\theta_a)e^{i\phi_a} & -\sin(\theta_a)e^{-i\psi_a} \\ \sin(\theta_a)e^{i\psi_a} & \cos(\theta_a)e^{-i\phi_a} \end{bmatrix}. \quad (4)$$

There is the possibility that the SFG efficiency of each of the two crystals is not perfectly matched, which can be modeled similarly to the imbalance in the modulator interferometer:

$$U_{\text{crys}} = N_{\text{crys}} \begin{bmatrix} \cos \theta_{\text{crys}} & 0 \\ 0 & \sin \theta_{\text{crys}} \end{bmatrix}, \quad (5)$$

where, again, we renormalize (via N_{crys}) to maintain unit total probability. As before, this step is state dependent.

At this point, the states exiting the source would ideally be aligned with the desired H, V, D, and A states. Finally, the fibers leading from the source to the transmitter will cause an additional arbitrary rotation of the states:

$$U_b = \begin{bmatrix} \cos(\theta_b)e^{i\phi_b} & -\sin(\theta_b)e^{-i\psi_b} \\ \sin(\theta_b)e^{i\psi_b} & \cos(\theta_b)e^{-i\phi_b} \end{bmatrix}. \quad (6)$$

The final density matrices of the states at the transmitter are thus

$$\rho'_x = U_b U_{\text{crys}} U_a R U_{\text{mod}} U_{\text{ph},x} \rho_D U_{\text{ph},x}^\dagger U_{\text{mod}}^\dagger R^\dagger U_a^\dagger U_{\text{crys}}^\dagger U_b^\dagger, \quad (7)$$

TABLE II: Purity and fidelity of the predicted post-compensation polarization states. Larger deviations are evident for the V and D states.

Expected state	Purity	Fidelity
H	0.9952	0.9839
V	0.7867	0.8705
D	0.8900	0.9337
A	0.9960	0.9835
Mean	0.9170	0.9429

TABLE III: Parameters used to model the state at the output of the transmitter. The crystals showed a significant imbalance (θ_{crys}), resulting in a non-unitary degradation of the polarizations states which cannot be corrected by the polarization compensation system. Additionally, two modulator phases (ϕ_V and ϕ_D) showed a notable deviation from the desired values. While the in-fiber unitary from the modulator to the crystals (θ_a , ϕ_a and ψ_a) and the in-fiber unitary from the crystals to the output of the transmitter (θ_b , ϕ_b and ψ_b) each showed deviations away from ideal, both of these operations are unitary and can therefore, in principle, be compensated by the polarization compensation system. The rightmost column indicates whether the parameter corresponds to a unitary rotation that can in principle be corrected by the polarization compensation system.

Parameter	Ideal value		Modeled value	Correctable
	Analytic	Numeric approx.		
ϕ_H	$\pi/2$	1.5708	1.5953	No
ϕ_V	$-\pi/2$	-1.5708	-1.4603	No
ϕ_D	0	0	-0.1227	No
ϕ_A	π	3.1416	3.0802	No
θ_{mod}	$\pi/4$	0.7854	0.7977	No
θ_a	0	0	1.1045	Yes
ϕ_a	0	0	0.0245	Yes
ψ_a	0	0	3.0925	Yes
θ_{crys}	$\pi/4$	0.7854	0.9695	No
θ_b	0	0	1.1024	Yes
ϕ_b	0	0	3.1170	Yes
ψ_b	0	0	-3.1907	Yes

with the two renormalizations applied at the appropriate stages.

With this representation, we vary the 9 free parameters to maximize the fidelity of our modeled output polarization states with the states measured at the transmitter by the polarization compensation system. The parameters that provided the highest overall fidelity are compared to the ideal values desired for 0% intrinsic QBER in Table III. From this it is clear that a significant contribution of the intrinsic QBER is due to an imbalance in the SFG efficiency, with one crystal showing a normalized efficiency of 70% compared to 30% in the other crystal, a difference of more than a factor 2. In addition, the phases (ϕ_V and ϕ_D) show notable deviations from the desired

values, explaining the lower fidelities measured in these two states (V and D) when compared to the other two states (H and A; see Table II). The parameters of the two arbitrary fiber unitaries also show significant deviations, but these are unitary rotations, common to all states, and thus the polarization compensation system could correct them if the other parameters were at the desired values. Non-ideal parameters in the optimized model would lead to uncorrectable non-unitary effects exhibited in the apparatus.

Another important effect that increased the intrinsic QBER is the reduced purity of the state (see Table II). This reduced purity may have been caused by unstable phase modulators, or unstable voltages applied to the modulators, in one polarity—the states with lower purity, V and D, correspond to different applied voltage polarities than the states with higher purity, H and A [1]. Other possible causes are spreading of the polarization components due to birefringence (given the short temporal width of the pulses), frequency-hopping of the 1550 nm laser, and noise due to background light.

We can model the purity reduction by adding a depolarizing channel [2] to the modeled states:

$$\rho_x'' = \left(\sqrt{2p_x - 1}\right) \rho_x' + \left(1 - \sqrt{2p_x - 1}\right) \frac{I}{2}, \quad (8)$$

where ρ_x'' is the modeled density matrix of the state x at the transmitter after accounting for reduced purity, p_x is the measured purity of the state and I is the identity matrix. Accounting for this reduced purity, our modeled states predict an intrinsic QBER of 5.33%, comparable to the 5.35% predicted by the polarization compensation system.

* Electronic address: jbourgoin@uwaterloo.ca, thomas.jennewein@uwaterloo.ca

- [1] Z. Yan, E. Meyer-Scott, J.-P. Bourgoin, B. L. Higgins, N. Gigov, A. MacDonald, H. Hübel, and T. Jennewein, *J. Lightwave Technol.* **31**, 1399 (2013).
- [2] M. A. Nielsen and I. L. Chuang, *Quantum Computation and Quantum Information* (Cambridge University Press, 2010).